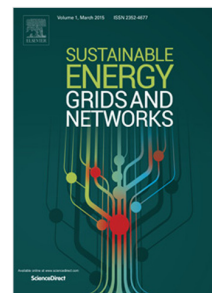


## Accepted Manuscript

Submission to Sustainable Energy, Grid and Network Journal Stability of Renewable Energy based Microgrid in Autonomous Operation

Awan Uji Krismanto, Nadarajah Mithulananthan, Olav Krause



PII: S2352-4677(17)30185-6  
DOI: <https://doi.org/10.1016/j.segan.2017.12.009>  
Reference: SEGAN 134

To appear in: *Sustainable Energy, Grids and Networks*

Received date: 4 August 2017  
Revised date: 1 December 2017  
Accepted date: 21 December 2017

Please cite this article as: A.U. Krismanto, N. Mithulananthan, O. Krause, Submission to Sustainable Energy, Grid and Network Journal Stability of Renewable Energy based Microgrid in Autonomous Operation, *Sustainable Energy, Grids and Networks* (2017), <https://doi.org/10.1016/j.segan.2017.12.009>

This is a PDF file of an unedited manuscript that has been accepted for publication. As a service to our customers we are providing this early version of the manuscript. The manuscript will undergo copyediting, typesetting, and review of the resulting proof before it is published in its final form. Please note that during the production process errors may be discovered which could affect the content, and all legal disclaimers that apply to the journal pertain.

## Submission to Sustainable Energy, Grid and Network Journal

## Stability of Renewable Energy based Microgrid in Autonomous Operation

Awan Uji Krismanto<sup>1</sup>, Nadarajah Mithulananthan<sup>1\*</sup>, Olav Krause<sup>1</sup><sup>1</sup> University of Queensland, Brisbane, Australia

a.krismanto@uq.edu.au, \*mithulan@itee.uq.edu.au, o.krause@uq.edu.au

**Abstract:** This paper develops a comprehensive small-signal model of hybrid renewable-energy-based microgrid (MG) in an attempt to perceive oscillatory stability performance and capture the potential interaction between low-frequency critical modes within the MG. Trajectories of sensitive modes due to controller gain variations were evaluated in order to determine the stability boundaries. It was noticeable that various power-sharing schemes significantly influenced the small-signal stability of MG. Moreover, modal interaction emerged due to the proximity of RES-based DG units and non-linear dynamic behaviour of the sensitive modes. The interaction may result in a more oscillatory situation which potentially leads to instability of MG. The low-frequency critical modes obtained from eigenvalues analysis were then verified with the help of nonlinear time domain simulations. The presented work contributes to enhance the design and tuning of controller gain and proposes appropriate power-sharing scheme within MG.

**Index Terms**—Renewable MG, small-signal stability, eigenvalues, modal interaction.

13

**Nomenclatures:**

Notations of variables in the proposed MG model are given as follows:

**Line and Load**

$i_{lIkDQ}$ ,  $D$  and  $Q$  axis line current.  
 $i_{lODQ}$   $D$  and  $Q$  axis load current.  
 $v_{bKdQ}$   $D$  and  $Q$  axis local bus voltage.

**Bio-Diesel (BDG) Generator**

$i_{kq1}, i_{kq2}$   $q$  axis rotor current.  
 $i_{kd}$   $d$  axis rotor current.  
 $i_{sdq}$   $d$  and  $q$  axis stator current.  
 $i_{fd}$   $d$  axis field winding current.  
 $T_{Mde}$  Mechanical torque.  
 $v_{fd}$   $d$  axis field winding voltage.  
 $v_{sdq}$   $d$  and  $q$  axis stator voltage.  
 $\omega_{ref}$  Angular frequency.  
 $\delta_d$  Phase angle.

**Two-stages PV system**

$i_b$  DC/DC converter input current.  
 $i_s$  DC/DC converter output current.

**Two-stages PV system**

$i_b$  DC/DC converter input current.  
 $i_s$  DC/DC converter output current.  
 $v_b$  DC/DC converter output voltage.  
 $v_{dc}$  DC link/ DC side voltage of DC/AC inverter.  
 $\rho_{pv}$  auxiliary control variables of DC/DC converter  
 $\delta_{pv}$  Phase angle of PV system.  
 $p_{pv}$  Active power of PV system.  
 $q_{pv}$  Reactive power of PV system.  
 $\varphi_{dq}$  Voltage control loop state variables.  
 $\beta_{dq}$  Current control loop state variables.  
 $i_{idq}$   $d$  and  $q$  axis DC/AC inverter current.  
 $v_{odq}$   $d$  and  $q$  axis output voltage.  
 $i_{odq}$   $d$  and  $q$  axis output current.  
 $i_{opvDQ}$   $D$  and  $Q$  axis PV output current in common reference frame.  
 $v_g$  Input voltage of PV system.  
 $n_p$  PV active power droop gain.  
 $n_q$  PV reactive power droop gain.

**Wind Energy Conversion System (WECS)**

Induction generator  
 $i_{sdq}$   $d$  and  $q$  axis stator current.

$i_{rdq}$   $d$  and  $q$  axis rotor current.  
 $\omega_w$  Angular frequency.  
 $v_{sdq}$   $d$  and  $q$  axis stator voltage.  
 $v_{sdq}$   $d$  and  $q$  axis stator voltage.  
 $v_{rdq}$   $d$  and  $q$  axis rotor voltage.  
 $\gamma$  Variable of reference current calculation in Flux Oriented Control (FOC).  
 $\rho_{wdq}$  FOC state variables.  
 $i_{indq}$   $d$  and  $q$  AC/DC converter current.  
 $v_{dqin}$   $d$  and  $q$  input voltage of AC/DC converter.  
 $\delta_w$  Phase angle of WECS.  
 $p_w$  Active power of WECS system.  
 $q_w$  Reactive power of WECS system.  
 $\varphi_{wdq}$  Voltage control loop state variables.  
 $\beta_{wdq}$  Current control loop state variables.  
 $i_{iwdq}$   $d$  and  $q$  axis DC/AC inverter current.  
 $v_{owdq}$   $d$  and  $q$  axis output voltage.  
 $i_{owdq}$   $d$  and  $q$  axis output current.  
 $v_{sdq}$   $d$  and  $q$  axis stator voltage.  
 $v_{rdq}$   $d$  and  $q$  axis rotor voltage.  
 $T_w$  Mechanical torque.

## 1. Introduction

The penetration of renewable energy resources (RES) based distributed generation (DG) has been increasing intensively in recent years due to their beneficial impacts in bringing clean energy and lowering the dependency on fossil fuel. Among various RES, photovoltaic (PV) and wind energy conversion system (WECS) have been considered as the most deployed DG units due to their favourable technical and economic benefits [1, 2]. On the other hand, the major concern in developing stand-alone PV or WECS based power generations is how to maintain the continuity of electricity supply. These concerns not only influence reliability of electricity supply but also require over-sizing of energy storage system (ESS) to manage with frequent early discharge due to RES fluctuations [3]. According to the limitations of individual DG unit, it is necessary to organize a cluster of DG units into a single controlled and coordinated power system known as Microgrid (MG).

Similar to the conventional power system, the stabilities issues in MG can be classified into transient, voltage and small signal stability. Transient stability concern in MG corresponded to the ability of MG to maintain a stable condition after being subjected to large disturbances such as short-circuit faults, structural change in MG due to the outage of a particular DG unit and operation mode switching from grid connected to islanding operation [4]. Transient instability problem is not a big concern in MG as the generating units considered are relatively small and mostly not synchronous machine based. MG should be able to maintain acceptable voltages at all buses under normal condition and after being exposed to a disturbance. Voltage stability problem in MG mostly emerges due to the connection of dynamic loads, reactive power limit and tap changer operation [5]. Moreover, the MG is susceptible to the occurrence of small perturbations as a consequence of having a cluster of RES based DG units with less physical inertia. Lack of system damping condition in a MG might lead to the undamped oscillatory condition when it is subjected to small disturbances such as fluctuating RES condition, small load change and parameter variations [5-9]. Therefore, a comprehensive study of small-signal stability in MG is crucial to ensure stable operation of MG.

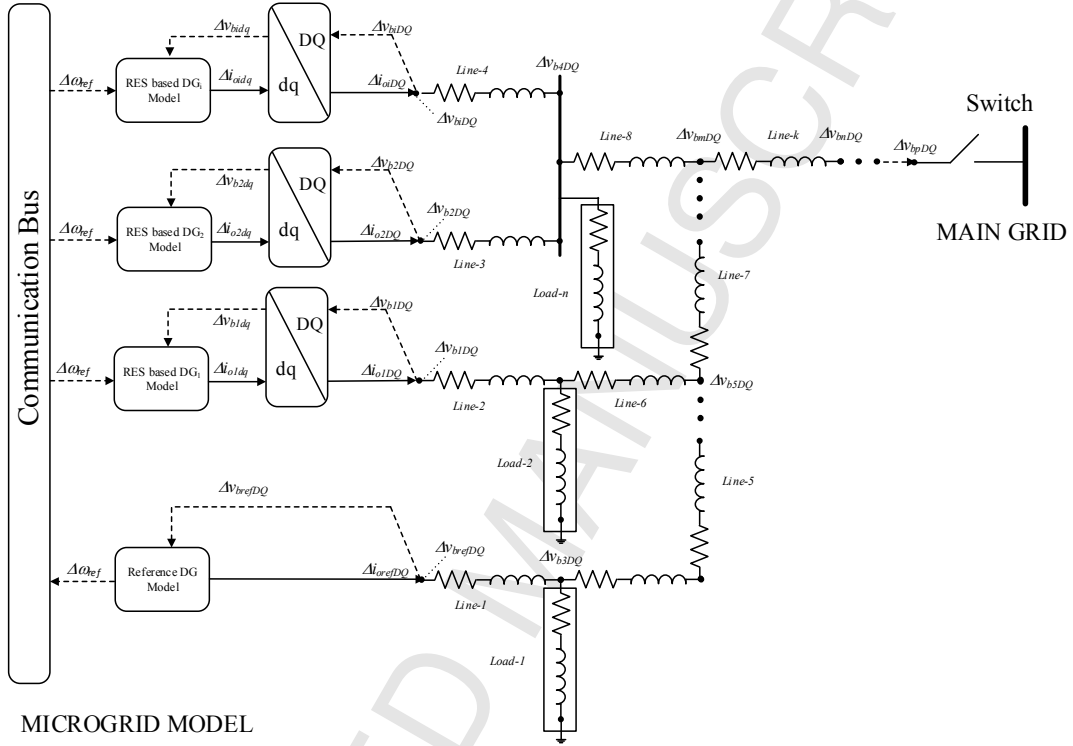
A limited amount of small-signal stability analysis considering different RES based DE units in MG was presented in the literature so far. In [10, 11], the small-signal stability analysis of wind-based MG was provided. However, the presented analysis neglected WECS dynamical behaviour and control system. In previous small-signal stability studies, power electronic devices in DG units are usually presented as an ideal voltage source which may lead to inaccurate results [12-14]. Practically, various architectures of power electronic devices are employed to get the most advantages from the RES. Therefore, different dynamic responses of DG units might emerge when various RES-based power generations are integrated into a MG. Those typical dynamic behaviours cannot be captured by using the simplified model as developed in the previous literature. A comprehensive MG model considering all possible dynamics from each of the DG units is required to provide a complete picture of small-signal stability of MG. Moreover, in a MG with a cluster of DG units, the interaction among sensitive eigenvalues potentially exhibit. Investigation of modal interaction is needed since the occurrence of interaction introduces more oscillatory conditions and deterioration of stability performance.

Detailed MG model was primarily developed in [15]. However, the control systems were not considered in the research. Hence, this paper develops a detailed model of each DG unit in MG to provide a comprehensive study and better understanding of MG small-signal stability performance under autonomous operation. A hybrid MG consists of WECS, PV and Bio-Diesel (BDG) generator is considered in this work. Trajectories of the low-frequency critical modes on different power sharing strategies and gain control variations are mapped to determine the small-signal stability boundaries. Moreover, the possibility of modal interaction between nearby eigenvalues is thoroughly analysed.

59 Time-domain simulation is then performed to verify and visualize the trajectories of eigenvalues  
60 analysis.

61 Rest of the paper is organized as follows. A step-by-step comprehensive modelling of PV-Wind-  
62 Diesel MG for small-signal investigation and a general summary of MG modelling is presented in  
63 Section 2, along with a brief methodology of small-signal stability and modal interaction. Section 3  
64 describes the simulation results in details. Conclusions and contributions of this paper are highlighted  
65 in Section 4.

## 66 2. State-Space Model of Hybrid Microgrid



67  
68 Fig.1 Typical MG structure in a distribution network.

69 Fig.1 represents a typical model of MG system in a generic distribution network. Under islanding  
70 mode, a synchronized operation is mandatory to maintain a stable MG operation. Therefore, it is  
71 necessary to translate all individual reference frame ( $dq$ ) of each DG unit into a common reference  
72 frame (DQ) which is provided by a reference DG unit. The reference DG can be performed by a  
73 synchronous machine based DG such as bio diesel generator (BDG) or an inverter based DG equipped  
74 with the controller to establish a given voltage magnitude and frequency [17]. Translation from the  
75 individual to the common reference frame is facilitated using transformation matrices of  $\mathbf{T}_c$  and  $\mathbf{T}_{co}$ .  
76 While, reverse transformation is conducted using inverse transformation matrices of  $\mathbf{T}_v$  and  $\mathbf{T}_{vs}$  [16].

77 Bus voltages are considered as input variables that provide a connection to each subsystem. The  
78 bus voltages ( $\Delta v_{kDQ}$ ) can be accurately estimated using the following equation [16]

$$79 \quad \Delta v_{kDQ} = R_N (\Delta i_{oDQ}) - R_N (\Delta i_{loDQ}) + R_N \left\{ (\Delta i_{likDQ})_{in} - (\Delta i_{likDQ})_{out} \right\} \quad (1)$$

80 Where  $R_N$  is virtual resistance,  $\Delta i_{oDQ}$  represents the output current of DG unit connected to the bus.  
81  $\Delta i_{loDQ}$  is related to the load current at bus  $k$ . While the  $(\Delta i_{likDQ})_{in}$  and  $(\Delta i_{likDQ})_{out}$  corresponding to a given line  
82 current entering and leaving the  $k^{\text{th}}$  bus, respectively.

83 In the following sections, modelling procedure of line impedances, load, and the DG units are  
84 presented. A comprehensive state-space model of BDG, two-stages PV and fully-rated WECS based

85 DG units are developed to examine a complete small-signal stability performance of islanding MG  
86 operation.

87

### 88 A. State-space Model of Line Impedances

89 Distribution lines presented in Fig.1 are modelled as series RL elements. The linearized state-  
90 space equations of line impedance between  $m$  and  $n$  nodes is given in (2) a generalized form.

$$91 \quad \Delta \dot{\mathbf{x}}_{\text{line}} = \mathbf{A}_{\text{line}} \Delta \mathbf{x}_{\text{line}} + \mathbf{B}_{\text{line1}} \Delta \mathbf{v}_{\text{mDQ}} + \mathbf{B}_{\text{line2}} \Delta \mathbf{v}_{\text{nDQ}} + \mathbf{B}_{\text{oli}} \Delta \omega_{\text{ref}} \quad (2)$$

92 Where  $\Delta \mathbf{x}_{\text{line}} = [\Delta i_{\text{likD}} \quad \Delta i_{\text{likQ}}]^T$ ,  $\Delta \mathbf{v}_{\text{mDQ}} = [\Delta v_{\text{mD}} \quad \Delta v_{\text{mQ}}]^T$ ,  $\Delta \mathbf{v}_{\text{nDQ}} = [\Delta v_{\text{nD}} \quad \Delta v_{\text{nQ}}]^T$ ,

$$93 \quad \mathbf{A}_{\text{line}} = \begin{bmatrix} -R_{\text{lik}}/L_{\text{lik}} & \omega_0 \\ -\omega_0 & -R_{\text{lik}}/L_{\text{lik}} \end{bmatrix}, \mathbf{B}_{\text{line1}} = \begin{bmatrix} 1/L_{\text{lik}} & 0 \\ 0 & 1/L_{\text{lik}} \end{bmatrix}, \mathbf{B}_{\text{line2}} = \begin{bmatrix} -1/L_{\text{lik}} & 0 \\ 0 & -1/L_{\text{lik}} \end{bmatrix}, \mathbf{B}_{\text{oli}} = \begin{bmatrix} I_{\text{lik0Q}} \\ -I_{\text{lik0D}} \end{bmatrix}.$$

94 The  $\Delta \omega_{\text{ref}}$  corresponds to the reference angular frequency from the reference DG unit. While,  $I_{\text{lik0D}}$  and  
95  $I_{\text{lik0Q}}$  represent the initial condition of line in common D and Q axis reference frame, respectively.

96 Coupling between DG units, lines impedance and load is provided by local bus voltages equation  
97 as given in (1). By substituting (1) to (2), a complete state-space model of line impedance can be  
98 derived as shown in (3).

$$99 \quad \Delta \dot{\mathbf{x}}_{\text{line}} = \{ \mathbf{A}_{\text{line}} + R_N (\mathbf{B}_{\text{line1}} - \mathbf{B}_{\text{line2}}) \} \Delta \mathbf{x}_{\text{line}} + \mathbf{B}_{\text{liDG}} \Delta \mathbf{i}_{\text{oDQ}} + \mathbf{B}_{\text{liio}} \Delta \mathbf{i}_{\text{loDQ}} + \mathbf{B}_{\text{oli}} \Delta \omega_{\text{ref}} \quad (3)$$

100 Where  $\mathbf{B}_{\text{liDG}} = \mathbf{B}_{\text{liio}} = R_N (\mathbf{B}_{\text{line1}} - \mathbf{B}_{\text{line2}})$ . The  $\mathbf{B}_{\text{liDG}}$ ,  $\mathbf{B}_{\text{liio}}$  and  $\mathbf{B}_{\text{oli}}$  represent connection matrices between line and  
101 corresponded DG units, load and reference DG respectively.

### 102 B. State-space Model of Static Load

103 A load impedance model consists of load resistance ( $R_{\text{lo}}$ ) and inductance ( $L_{\text{lo}}$ ) is developed to  
104 present an aggregated load in MG. In general, state equation of the  $m$ -th a central load is given by

$$105 \quad \Delta \dot{\mathbf{x}}_{\text{lo}} = \mathbf{A}_{\text{lo}} \Delta \mathbf{x}_{\text{lo}} + \mathbf{B}_{\text{vlo}} \Delta \mathbf{v}_{\text{mDQ}} + \mathbf{B}_{\text{olo}} \Delta \omega_{\text{ref}} \quad (4)$$

$$106 \quad \text{Where } \Delta \mathbf{x}_{\text{lo}} = [\Delta i_{\text{lomD}} \quad \Delta i_{\text{lomQ}}]^T, \mathbf{A}_{\text{lo}} = \begin{bmatrix} -R_{\text{lom}}/L_{\text{lom}} & \omega_0 \\ -\omega_0 & -R_{\text{lom}}/L_{\text{lom}} \end{bmatrix}, \mathbf{B}_{\text{vlo}} = \begin{bmatrix} -1/L_{\text{lom}} & 0 \\ 0 & -1/L_{\text{lom}} \end{bmatrix}, \mathbf{B}_{\text{olo}} = \begin{bmatrix} I_{\text{lomQ}} \\ -I_{\text{lomD}} \end{bmatrix}. R_{\text{lom}} \text{ and } L_{\text{lom}}$$

107 represent resistance and inductance of line respectively.

108 The coupling between load, DG unit and distribution line is represented by bus voltage equation as  
109 given in (1). By substituting (1) to (4), the load state equation can be rewritten as

$$110 \quad \Delta \dot{\mathbf{x}}_{\text{lo}} = \{ \mathbf{A}_{\text{lo}} + R_N \mathbf{B}_{\text{vlo}} \} \Delta \mathbf{x}_{\text{lo}} + \mathbf{B}_{\text{loDG}} \Delta \mathbf{i}_{\text{oDQ}} + \mathbf{B}_{\text{loli}} \Delta \mathbf{i}_{\text{liDQ}} + \mathbf{B}_{\text{olo}} \Delta \omega_{\text{ref}} \quad (5)$$

111 Where  $\mathbf{B}_{\text{loDG}} = \mathbf{B}_{\text{loli}} = R_N \mathbf{B}_{\text{vlo}}$ . The  $\mathbf{B}_{\text{loDG}}$ ,  $\mathbf{B}_{\text{loli}}$  and  $\mathbf{B}_{\text{olo}}$  represent connection matrices between load and  
112 corresponded DG units, line and reference DG respectively.

### 113 C. State-space Model of Bio-Diesel generator (BDG)

114 The BDG is modelled as a permanent-magnet synchronous generator. In this research, the BDG  
115 is integrated to the hybrid MG as a reference DG unit which is responsible for providing a  
116 synchronization signal for other DG units and ensures the balanced condition of power generation and  
117 power consumption when there is a shortfall of energy from RES based DG units. The state-space  
118 model of BDG is derived from [18, 19].

119 State variables of the BDG involved two  $q$  axis ( $i_{\text{kq12}}$ ) and one  $d$  axis ( $i_{\text{kd}}$ ) rotor currents, stator  
120 current ( $i_{\text{sdq}}$ ) and field winding currents ( $i_{\text{fd}}$ ). Input variables are presented as mechanical torque ( $T_{\text{MDE}}$ ),



Fig.2. DC/DC Converter control. Fig.3. Droop control of PV system DC/AC inverter [16].

Auxiliary state equation ( $\rho_{pv}$ ) of the proposed DC/DC controller loop is given by

$$\frac{d\Delta\rho_{pv}}{dt} = v_{dc\_ref} - v_{dc} \quad (8)$$

The controller generates a control signal for DC/DC converter. The state-space equation of DC/DC controller is given in (9).

$$\begin{aligned} \Delta\dot{\rho}_{pv} &= [0]\Delta\rho_{pv} + [1 \quad -1] \begin{bmatrix} \Delta v_{dc\_ref} \\ v_{dc} \end{bmatrix} \\ \Delta d_{pv} &= [K_{ipv}]\Delta\rho_{pv} + [K_{ppv} \quad -K_{ppv}] \begin{bmatrix} \Delta v_{dc\_ref} \\ v_{dc} \end{bmatrix} \end{aligned} \quad (9)$$

Where ( $\Delta v_{dc\_ref}$ ) represents the DC link reference voltage.

Controller of DC/AC grid-side inverter in Fig.3 can be divided into droop control, outer voltage and inner current control loops [16, 23]. Droop control method is employed to establish a power sharing for each DG unit. The instantaneous output power in a certain operating point is determined by linearizing the calculated instantaneous power as given by the following equations:

$$\begin{aligned} \Delta p &= I_{od} \Delta v_{od} + I_{oq} \Delta v_{oq} + V_{od} \Delta i_{od} + V_{oq} \Delta i_{oq} \\ \Delta q &= I_{oq} \Delta v_{od} - I_{od} \Delta v_{oq} - V_{oq} \Delta i_{od} + V_{od} \Delta i_{oq} \end{aligned} \quad (10)$$

The average active ( $\Delta P$ ) and reactive ( $\Delta Q$ ) power are determined by employing first order low pass filter to the linearized instantaneous power as follows

$$\begin{aligned} \frac{d\Delta P}{dt} &= \omega_c \{ I_{od} \Delta v_{od} + I_{oq} \Delta v_{oq} + V_{od} \Delta i_{od} + V_{oq} \Delta i_{oq} \} - \omega_c \Delta P \\ \frac{d\Delta Q}{dt} &= \omega_c \{ I_{oq} \Delta v_{od} - I_{od} \Delta v_{oq} - V_{oq} \Delta i_{od} + V_{od} \Delta i_{oq} \} - \omega_c \Delta Q \end{aligned} \quad (11)$$

Where  $\omega_c$  represent cut off frequency of the low pass filter.

System frequency ( $\omega$ ) and active power sharing are set by active power droop gain ( $n_p$ ). While reference of  $d$ -axis voltage ( $v_{dq}^*$ ) and reactive power sharing is determined by reactive power droop gain ( $n_q$ ). It is assumed that  $q$ -axis component of voltage magnitude reference ( $\Delta v_{oq}^*$ ) is zero. In most of the cases, output impedance of the inverter is inductive around the fundamental frequency [24]. Hence the reference frequency and voltage are given by the following equations:

$$\begin{aligned} \omega &= \omega_n - n_p \Delta P \\ v_{od}^* &= V_n - n_q \Delta Q \end{aligned} \quad (12)$$

Where  $\omega_n$  and  $V_n$  represent nominal values of angular frequency and voltage respectively.

Phase angle ( $\delta$ ) between individual inverter reference frame and the common reference frame is determined from integral operation of the angular frequency ( $\omega$ ) [16]. By substituting (11) to (12), state-space equation of the droop controller can be determined as given in (13).

$$\begin{aligned} \begin{bmatrix} \Delta\dot{\delta} \\ \Delta\dot{p} \\ \Delta\dot{q} \end{bmatrix} &= \begin{bmatrix} 0 & 0 & 0 \\ 0 & -\omega_c & 0 \\ 0 & 0 & -\omega_c \end{bmatrix} \begin{bmatrix} \Delta\delta \\ \Delta p \\ \Delta q \end{bmatrix} + \begin{bmatrix} 0 & 0 & 0 & 0 \\ \omega_c I_{od} & \omega_c I_{oq} & \omega_c V_{od} & \omega_c V_{oq} \\ \omega_c I_{oq} & -\omega_c I_{od} & -\omega_c V_{oq} & \omega_c V_{od} \end{bmatrix} \begin{bmatrix} \Delta v_{odq} \\ \Delta i_{odq} \end{bmatrix} \\ \begin{bmatrix} \Delta\omega \\ \Delta v_{odq}^* \end{bmatrix} &= \begin{bmatrix} 0 & -n_p & 0 \\ 0 & 0 & -n_q \\ 0 & 0 & 0 \end{bmatrix} \begin{bmatrix} \Delta\delta \\ \Delta p \\ \Delta q \end{bmatrix} \end{aligned} \quad (13)$$

The obtained reference values from the power droop control are employed as input for voltage control loop. Auxiliary state equations ( $\varphi_d, \varphi_q$ ) of voltage control loop is given by (14).

$$\frac{d\varphi_d}{dt} = v_{od}^* - v_{od}, \quad \frac{d\varphi_q}{dt} = v_{oq}^* - v_{oq} \quad (14)$$

The algebraic equations of reference currents are determined as given by the following equations.

$$\begin{aligned} \Delta i_{od}^* &= G\Delta i_{od} - \omega_n C_f \Delta v_{oq} + K_{pv} (\Delta v_{od}^* - \Delta v_{od}) + K_{iv} \Delta \varphi_d \\ \Delta i_{oq}^* &= G\Delta i_{oq} + \omega_n C_f \Delta v_{od} + K_{pv} (\Delta v_{oq}^* - \Delta v_{oq}) + K_{iv} \Delta \varphi_q \end{aligned} \quad (15)$$

The linearized state equations of voltage control are derived from auxiliary state equation in (14) and the algebraic equations of the reference currents in (15) as given by (16).

$$\begin{bmatrix} \Delta \dot{\varphi}_d \\ \Delta \dot{\varphi}_q \end{bmatrix} = [0] \begin{bmatrix} \Delta \varphi_d \\ \Delta \varphi_q \end{bmatrix} + \begin{bmatrix} 1 & 0 & -1 & 0 \\ 0 & 1 & 0 & -1 \end{bmatrix} \begin{bmatrix} \Delta v_{od}^* \\ \Delta v_{oq}^* \end{bmatrix} \quad (16)$$

$$\begin{bmatrix} \Delta i_{id}^* \\ \Delta i_{iq}^* \end{bmatrix} = \begin{bmatrix} K_{iv} & 0 \\ 0 & K_{iv} \end{bmatrix} \begin{bmatrix} \Delta \varphi_d \\ \Delta \varphi_q \end{bmatrix} + \begin{bmatrix} K_{pv} & 0 & -K_{pv} & -\omega_n C_f & G & 0 \\ 0 & K_{pv} & \omega_n C_f & -K_{pv} & 0 & G \end{bmatrix} \begin{bmatrix} \Delta v_{od}^* \\ \Delta v_{oq}^* \\ \Delta i_{od}^* \\ \Delta i_{oq}^* \end{bmatrix}$$

The proportional and integral gains of voltage control loop are presented by  $K_{pv}$  and  $K_{iv}$  respectively. While, feed forward gain control is stated as  $G$ .

Output variables from the voltage control are then applied to the inner current controller as reference values. Auxiliary state equations ( $\beta_d, \beta_q$ ) of the current control loop as given by (17).

$$\frac{d\beta_d}{dt} = i_{od}^* - i_{od}, \quad \frac{d\beta_q}{dt} = i_{oq}^* - i_{oq} \quad (17)$$

The algebraic equations of current controller loop related to inverter modulation index is given by the following equation

$$\begin{aligned} m_d^* &= -\omega_n L_f \Delta i_{oq} + K_{pc} (\Delta i_{od}^* - \Delta i_{od}) + K_{ic} \Delta \beta_d \\ m_q^* &= \omega_n L_f \Delta i_{od} + K_{pc} (\Delta i_{oq}^* - \Delta i_{oq}) + K_{ic} \Delta \beta_q \end{aligned} \quad (18)$$

The linearized state equations of current control are derived from auxiliary state equation in (17) and the algebraic equations of the modulation index in (18) as given by (19).

$$\begin{aligned} \begin{bmatrix} \Delta \dot{\beta}_d \\ \Delta \dot{\beta}_q \end{bmatrix} &= [0] \begin{bmatrix} \Delta \beta_d \\ \Delta \beta_q \end{bmatrix} + \begin{bmatrix} 1 & 0 & -1 & 0 \\ 0 & 1 & 0 & -1 \end{bmatrix} \begin{bmatrix} \Delta i_{od}^* \\ \Delta i_{oq}^* \end{bmatrix} \\ \begin{bmatrix} \Delta m_d^* \\ \Delta m_q^* \end{bmatrix} &= \begin{bmatrix} K_{ic} & 0 \\ 0 & K_{ic} \end{bmatrix} \begin{bmatrix} \Delta \beta_d \\ \Delta \beta_q \end{bmatrix} + \begin{bmatrix} K_{pc} & 0 & -K_{pc} & -\omega_n L_f \\ 0 & K_{pc} & \omega_n L_f & -K_{pc} \end{bmatrix} \begin{bmatrix} \Delta i_{od}^* \\ \Delta i_{oq}^* \end{bmatrix} \end{aligned} \quad (19)$$

Where, the proportional and integral gains of current control loop are presented by  $K_{pc}$  and  $K_{ic}$  respectively.

A complete model of PV system is determined by combining state equations of DC/DC and DC/AC in [21, 25]. These converter models are then integrated into state-space equations of the DC link (9), power droop (13), voltage (16) and current (19) controllers. Eighteen state variables are considered to obtain a detailed model of two-stages PV based DG unit. Linearized state-space model of two-stages PV is given by

$$\begin{aligned} \Delta \dot{\mathbf{x}}_{pv} &= \mathbf{A}_{pv} \Delta \mathbf{x}_{pv} + \mathbf{B}_{pv} \Delta \mathbf{u}_{pv} + \mathbf{B}_{vpv} \Delta \mathbf{v}_{bvpv} + \mathbf{B}_{opv} \Delta \omega_{ref} \\ \Delta \mathbf{i}_{opvdq} &= [0_{2 \times 16} \quad \mathbf{I}_{2 \times 2}] \Delta \mathbf{x}_{pv} \end{aligned} \quad (20)$$

Where

$$\begin{aligned} \mathbf{u}_{pv} &= [\Delta v_g \quad \Delta v_{dc}^*]^T, \quad \Delta \mathbf{v}_{bvpv} = [\Delta v_{bpd} \quad \Delta v_{bpvq}]^T, \quad \Delta \mathbf{x}_{pv} = [\Delta i_b \quad \Delta i_s \quad \Delta v_b \quad \Delta v_{dc} \quad \Delta \rho_{pv} \quad \Delta \delta_{pv} \quad \Delta p_{pv} \quad \Delta q_{pv} \quad \Delta \varphi_{pvd} \quad \Delta \varphi_{pvq} \\ &\quad \Delta \beta_{pvd} \quad \Delta \beta_{pvq} \quad \Delta i_{id} \quad \Delta i_{iq} \quad \Delta v_{od} \quad \Delta v_{oq} \quad \Delta i_{od} \quad \Delta i_{oq}]^T \end{aligned}$$



204

$$\mathbf{B}_{pv} = \begin{bmatrix} \frac{1}{L_s} \frac{K_{ppv} (I_{b0} R_{cb} - I_{s0} R_{cb} + V_{b0})}{L_b} \\ 0 \\ 0 \\ 0_{15 \times 1} \end{bmatrix}, \mathbf{B}_{vpv} = \begin{bmatrix} 0_{16 \times 1} & 0_{16 \times 1} \\ -\frac{1}{L_c} & 0 \\ 0 & -\frac{1}{L_c} \end{bmatrix}, \mathbf{B}_{opv} = \begin{bmatrix} 0_{5 \times 1} \\ -1 \\ 0_{12 \times 1} \end{bmatrix}.$$

205

206

207

The synchronization signal for PV based DG unit is provided by BDG which is presented by  $\Delta\omega_{ref}$ .

By substituting  $\Delta\omega_{ref}$  values as given in (6), the state equations of PV based DG unit can be rewritten as

208

$$\begin{aligned} \dot{\Delta \mathbf{x}}_{pv} &= \mathbf{A}_{pv} \Delta \mathbf{x}_{pv} + \mathbf{B}_{pv} \Delta \mathbf{u}_{pv} + \mathbf{B}_{vpv} \Delta \mathbf{v}_{bpv} + \mathbf{B}_{opv} \mathbf{C}_{BDG2} \Delta \mathbf{x}_{BDG} \\ \Delta \mathbf{i}_{opvdq} &= [0_{2 \times 16} \quad \mathbf{I}_{2 \times 2}] \Delta \mathbf{x}_{pv} \end{aligned} \quad (21)$$

209

210

Output currents of PV system have to be aligned with common reference frame as given by

211

$$\Delta \mathbf{i}_{oDQ} = \mathbf{C}_{pvDQ} \Delta \mathbf{x}_{pv} \quad (22)$$

212

Where  $\mathbf{C}_{pvDQ} = [0_{2 \times 5} \quad \mathbf{T}_c \quad 0_{2 \times 10} \quad \mathbf{T}_f]$ .

213

214

215

The local bus voltage is one of the input variables for the state-space equations of PV based DG unit. Transformation of bus voltage variables from common to individual reference frame can be conducted by substituting (1) to (21) as given by

216

$$\begin{bmatrix} v_{bpvd} \\ v_{bpvq} \end{bmatrix} = \mathbf{T}_f^{-1} R_N \mathbf{C}_{pvDQ} \Delta \mathbf{x}_{pv} + \mathbf{T}_v [\Delta \delta_{pv}] - \mathbf{T}_f^{-1} R_N [\Delta \mathbf{i}_{oDQ}] + \mathbf{T}_f^{-1} R_N \left\{ [\Delta \mathbf{i}_{iDQ}]_{in} - [\Delta \mathbf{i}_{iDQ}]_{out} \right\} \quad (23)$$

217

218

219

By substituting (22) and (23) into (21) and considering that the  $\Delta\delta_{pv}$  part has been integrated to the state matrix of PV based DG unit, the complete state-space model of two-stages PV based DG can be stated as

220

$$\begin{aligned} \dot{\Delta \mathbf{x}}_{pv} &= \mathbf{A}_{pv,DG} \Delta \mathbf{x}_{pv} + \mathbf{B}_{pv} \Delta \mathbf{u}_{pv} + \mathbf{B}_{pvline} \Delta \mathbf{x}_{line} + \mathbf{B}_{pvload} \Delta \mathbf{x}_{load} + \mathbf{B}_{pv,BDG} \Delta \mathbf{x}_{BDG} \\ \Delta \mathbf{i}_{oDQ} &= \mathbf{C}_{pvDQ} \Delta \mathbf{x}_{pv} \end{aligned} \quad (24)$$

221

Where  $\mathbf{A}_{pv,DG} = \mathbf{A}_{pv} + R_N \mathbf{T}_f^{-1} \mathbf{B}_{vpv} \mathbf{C}_{pvDQ}$ ,  $\mathbf{B}_{pvline} = R_N \mathbf{T}_f^{-1} \mathbf{B}_{vpv}$ ,  $\mathbf{B}_{pvload} = R_N \mathbf{T}_f^{-1} \mathbf{B}_{vpv}$ ,  $\mathbf{B}_{pv,BDG} = \mathbf{B}_{opv} \mathbf{C}_{BDG2}$ .

222

### E. State-space Model of Fully Rated WECS

223

224

225

226

227

228

229

230

231

232

233

234

The fully rated WECS mainly consists of a wind turbine, induction or synchronous generator, back to back AC/DC/AC inverter and associated controllers. The two-stages AC/DC and DC/AC converter system facilitate the interface between generator and grid side of fully rated WECS while providing decoupling between those two elements. Hence, for small variation of wind power, the dynamics from the generator side due to wind fluctuation will not influence the dynamic of the grid. Moreover, the interfacing power electronic device is enabled to facilitate the variable speed operation capability of the generator which allows the effective regulation of voltage and power output [26]. Small-signal model of back to back AC/DC/AC inverter is obtained from integration of the subsystem in [22, 27] and [25]. While, the linearized induction generator model is derived from [18, 19]. A complete model of fully-rated WECS is determined by integrating the WECS state-space model in [15] with its associated controller. The controllers in fully-rated WECS is comprising of generator-side AC/DC converter and grid-side DC/AC inverter controllers.

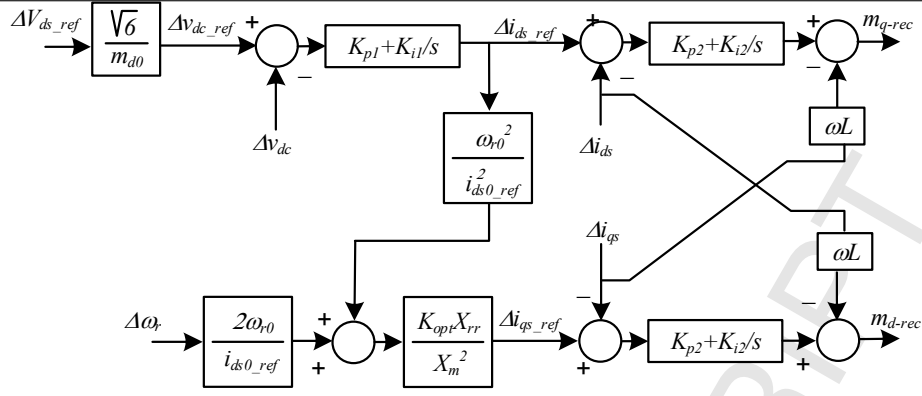


Fig. 4. FOC method for generator side converter [18, 28].

Flux oriented control (FOC) strategy as shown in Fig.4 is applied to the generator-side AC/DC converter to facilitate variable speed operation of induction generator, maintain generator voltage stability and perform DC link voltage regulation [28].

Reference of DC link voltage is determined from  $d$ -axis stator voltage reference value and nominal modulation index of AC/DC converter as given by [29]:

$$\Delta v_{dc\_ref} = \frac{\sqrt{6}}{m_{d0\_rec}} \Delta v_{ds\_ref} \quad (25)$$

The calculated reference values of DC link voltage is then compared with the measured DC link voltage and regulated through PI controller. Auxiliary variables ( $\gamma$ ) of the corresponded control loop is denoted by

$$\frac{d\gamma}{dt} = \Delta v_{dc\_ref} - \Delta v_{dc} \rightarrow \frac{d\gamma}{dt} = \frac{\sqrt{6}}{m_{d0}} \Delta v_{ds\_ref} - \Delta v_{dc} \quad (26)$$

State-space equation corresponded to the  $d$ -axis current reference ( $\Delta i_{ds}^*$ ) can be stated as

$$\begin{aligned} \begin{bmatrix} \Delta \dot{\gamma} \\ \Delta \dot{i}_{ds}^* \end{bmatrix} &= \begin{bmatrix} 0 \\ -1 \end{bmatrix} \Delta v_{dcout} + \begin{bmatrix} \frac{\sqrt{6}}{m_{d0}} \\ 0 \end{bmatrix} \Delta v_{ds\_ref} \\ \Delta \dot{i}_{ds}^* &= \begin{bmatrix} K_{i1} \\ -K_{p1} \end{bmatrix} \Delta \gamma + \begin{bmatrix} 0 \\ -1 \end{bmatrix} \Delta v_{dcout} + \begin{bmatrix} \frac{\sqrt{6}}{m_{d0}} \\ 0 \end{bmatrix} \Delta v_{ds\_ref} \end{aligned} \quad (27)$$

The quadrature axis,  $q$  reference current ( $\Delta i_{qs}^*$ ) is derived from torque-speed characteristic curve[18]. Electromagnetic torque equation can be simplified by assuming that rotor flux of induction generator is aligned to the direct axis ( $\psi = 0$ ) and optimal operation of a wind turbine is attained [28].

The linearized  $q$ -axis reference current can be stated as

$$\Delta i_{qs}^* = \left( \frac{2\omega_{r0} K_{opt} X_{rr}}{i_{d0s}^* X_m^2} \right) \Delta \omega_r + \left( \frac{K_{i1} K_{opt} \omega_{r0}^2 X_{rr}}{(i_{d0s}^*)^2 X_m^2} \right) \Delta \gamma - \left( \frac{K_{p1} K_{opt} \omega_{r0}^2 X_{rr}}{(i_{d0s}^*)^2 X_m^2} \right) \Delta v_{dcout} + \left( \frac{K_{p1} K_{opt} \omega_{r0}^2 X_{rr} \sqrt{6}}{(i_{d0s}^*)^2 X_m^2 m_{d0}} \right) \Delta v_{ds\_ref} \quad (28)$$

Reference currents are compared to measured  $dq$  axis stator current and regulated by PI controller to generate a control signal for AC/DC converter ( $m_{dq}^*$ ). Auxiliary variables ( $\rho_{wdq}$ ) for calculating modulation indices of the AC/DC converter is denoted by

$$\frac{d\rho_{wd}}{dt} = i_{sd}^* - i_{sd}, \quad \frac{d\rho_{wq}}{dt} = i_{sq}^* - i_{sq} \quad (29)$$

By integrating (27), (28) and (29), state-space equations of FOC are given by

$$\begin{bmatrix} \Delta \dot{\rho}_{wd} \\ \Delta \dot{\rho}_{wq} \end{bmatrix} = \begin{bmatrix} 0 & 0 \\ 0 & 0 \end{bmatrix} \begin{bmatrix} \Delta \rho_{wd} \\ \Delta \rho_{wq} \end{bmatrix} + \mathbf{B}_{\text{IFOC}} \begin{bmatrix} i_{sd} \\ i_{sq} \\ \Delta \gamma \\ \Delta v_{dc} \\ \Delta \omega \end{bmatrix} + \mathbf{B}_{\text{2FOC}} [\Delta v_{sd}^*] \quad (30)$$

$$\begin{bmatrix} \Delta m_{1d} \\ \Delta m_{1q} \end{bmatrix} = \begin{bmatrix} K_{i2} & 0 \\ 0 & K_{i2} \end{bmatrix} \begin{bmatrix} \Delta \rho_{wd} \\ \Delta \rho_{wq} \end{bmatrix} + \mathbf{D}_{\text{FOC1}} \begin{bmatrix} \Delta i_{sd}^* \\ \Delta i_{sq}^* \\ \Delta i_{sd} \\ \Delta i_{sq} \end{bmatrix} + \mathbf{D}_{\text{FOC2}} [\Delta \omega_r] + \mathbf{D}_{\text{FOC3}} [\Delta v_{sd}^*]$$

$$\text{Where } \mathbf{B}_{\text{IFOC}} = \begin{bmatrix} -1 & 0 & K_{i1} & -K_{p1} & 0 \\ 0 & -1 & \frac{K_{i1} K_{opt} \omega_{r0}^2 X_r}{(i_{sd0}^*)^2 X_m^2} & -\frac{K_{p1} K_{opt} \omega_{r0}^2 X_r}{(i_{sd0}^*)^2 X_m^2} & \frac{2\omega_{r0}^2 K_{opt} X_r}{(i_{sd0}^*)^2 X_m^2} \end{bmatrix}, \mathbf{B}_{\text{FOC2}} = \begin{bmatrix} \frac{K_{p1} \sqrt{6}}{m_{1d0}} \\ \frac{K_{p1} K_{opt} \omega_{r0}^2 X_r \sqrt{6}}{(i_{sd0}^*)^2 X_m^2 m_{1d0}} \end{bmatrix},$$

$$\mathbf{D}_{\text{FOC1}} = \begin{bmatrix} -K_{p2} & -\omega L & K_{i1} & -K_{p1} K_{p2} \\ \omega L & -K_{p2} & \frac{K_{i1} K_{p2} K_{opt} \omega_{r0}^2 X_r}{(i_{sd0}^*)^2 X_m^2} & -\frac{K_{p1} K_{p2} K_{opt} \omega_{r0}^2 X_r}{(i_{sd0}^*)^2 X_m^2} \end{bmatrix}, \mathbf{D}_{\text{FOC2}} = \begin{bmatrix} 0 \\ \frac{2\omega_{r0} K_{p2} K_{opt} X_r}{(i_{sd0}^*)^2 X_m^2} \end{bmatrix}, \mathbf{D}_{\text{FOC3}} = \begin{bmatrix} \frac{K_{i1} K_{p2} \sqrt{6}}{m_{1d0}} \\ \frac{K_{p1} K_{p2} K_{opt} \omega_{r0}^2 X_r \sqrt{6}}{(i_{sd0}^*)^2 X_m^2 m_{1d0}} \end{bmatrix}$$

Similar control algorithm as in two-stage PV system is adopted in WECS DC/AC inverter control. A complete state-space model for fully rated WECS is then derived from the integration of induction generator model [18, 19], AC/DC/AC inverter model [25, 27], generator side (FOC) controller in (27) and (30), and grid side controller (13), (16) and (19). Twenty-eight state variables are considered to determine a detailed model of WECS-based DG unit. Linearized state equations of WECS are given by in (31).

$$\begin{aligned} \Delta \dot{\mathbf{x}}_w &= \mathbf{A}_w \Delta \mathbf{x}_w + \mathbf{B}_w \Delta \mathbf{u}_w + \mathbf{B}_{vw} \Delta \mathbf{v}_{bw} + \mathbf{B}_{\omega w} \Delta \omega_{ref} \\ \Delta \mathbf{i}_{owdq} &= [0_{2 \times 26} \quad \mathbf{I}_{2 \times 2}] \Delta \mathbf{x}_w \end{aligned} \quad (31)$$

$$\text{Where } \Delta \mathbf{u}_w = [\Delta v_{sd} \quad \Delta v_{sq} \quad \Delta v_{rd} \quad \Delta v_{rq} \quad \Delta T_w \quad \Delta v_{sd}^*]^T, \Delta \mathbf{v}_{bw} = [\Delta v_{bwd} \quad \Delta v_{bwq}]^T,$$

$$\Delta \mathbf{x}_w = \begin{bmatrix} \Delta i_{sd} & \Delta i_{sq} & \Delta i_{rd} & \Delta i_{rq} & \Delta \omega_r & \Delta \gamma & \Delta \rho_{wd} & \Delta \rho_{wq} \\ \Delta i_{id} & \Delta i_{iq} & \Delta v_{din} & \Delta v_{qin} & \Delta v_{dcout} & \Delta \delta & \Delta p & \Delta q & \Delta \phi_d & \Delta \phi_q \\ \Delta \beta_d & \Delta \beta_q & \Delta i_s & \Delta v_{dc} & \Delta i_{invd} & \Delta i_{invq} & \Delta v_{od} & \Delta v_{oq} & \Delta i_{od} & \Delta i_{oq} \end{bmatrix}^T, \mathbf{B}_{vw} = \begin{bmatrix} 0_{26 \times 1} & 0_{26 \times 1} \\ -\frac{1}{L_c} & 0 \\ 0 & -\frac{1}{L_c} \end{bmatrix}, \mathbf{B}_{\omega w} = \begin{bmatrix} 0_{13 \times 1} \\ -1 \\ 0_{14 \times 1} \end{bmatrix}. \text{ While, the}$$

detailed presentation of  $\mathbf{B}_w$  is derived from [18, 19].

The synchronization signal for WECS based DG unit is provided by BDG which is presented by  $\Delta \omega_{ref}$ . By substituting  $\Delta \omega_{ref}$  values as given in (6), the state equations of WECS based DG unit can be rewritten as

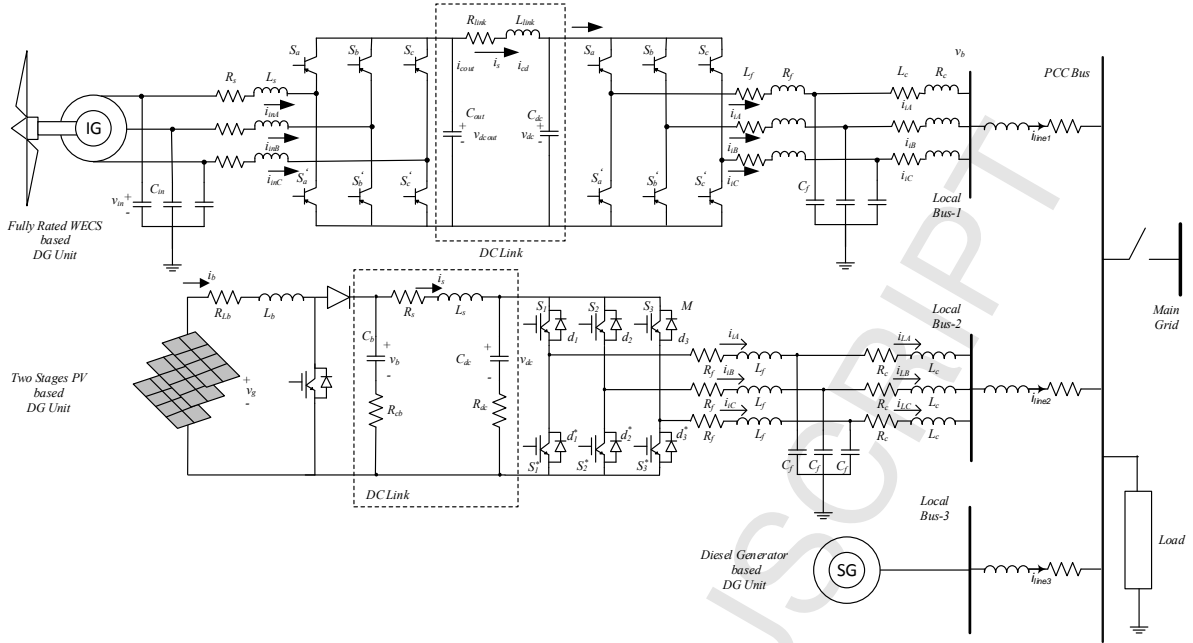
$$\begin{aligned} \Delta \dot{\mathbf{x}}_{pv} &= \mathbf{A}_{pv} \Delta \mathbf{x}_{pv} + \mathbf{B}_{pv} \Delta \mathbf{u}_{pv} + \mathbf{B}_{vpv} \Delta \mathbf{v}_{bvpv} + \mathbf{B}_{\text{opv}} \mathbf{C}_{\text{BDG2}} \Delta \mathbf{x}_{\text{BDG}} \\ \Delta \mathbf{i}_{\text{opvdq}} &= [0_{2 \times 16} \quad \mathbf{I}_{2 \times 2}] \Delta \mathbf{x}_{pv} \end{aligned} \quad (32)$$

Output currents of WECS have to be aligned to the common reference frame to facilitate synchronization with other DG unit. The transformation of WECS output current from individual to common reference frame is given by

$$\Delta \mathbf{i}_{\text{owDQ}} = \mathbf{C}_{\text{wDQ}} \Delta \mathbf{x}_w \quad (33)$$



## 313 3. Simulation Results



314 Fig.5 The test system of hybrid MG.  
315

316 A hybrid MG model consisting of three DG units; WECS, PV and BDG is investigated in this  
317 study as depicted in Fig.5. Two-stage converter system comprising of DC/DC and DC/AC formed a PV  
318 based DG unit. While, typical fully rated WECS incorporating DC/AC/DC converter was selected due  
319 to its superior characteristics in providing full power conversion and variable generator speed operation  
320 capability [28, 30]. Mitigation of high order harmonics of DG units' output current and voltage are  
321 handled by interfaced low pass filter. BDG is connected as a reference DG unit which provides a  
322 synchronization signal for other DG units and additional power when the generated power from PV and  
323 WECS are not sufficient to supply the load. In the investigated MG system, three line-impedances are  
324 considered to connect each DG unit with the single load bus. Moreover, an aggregated static load is  
325 considered in this study.

326 It is expected that the detailed MG model would provide more accurate results correlated to the  
327 ability of the proposed model to capture various dynamic response from different RES based DG units  
328 (WECS, PV and BDG). On the other hand, it is difficult to observe the typical dynamic behaviours  
329 from different DG unit architectures using simplified model as presented in the literature [5, 14, 16, 20,  
330 31-33]. The analysis of MG small signal stability using the simplified model results in similar dynamic  
331 responses for all the inverter based DG unit. Therefore, the simplified approach is not sufficient to  
332 present or to model a system with different type of RES based DG units.

### 333 A. Eigenvalues Analysis

334 A complete state-space model of hybrid MG was constructed. The capacity of each DG unit in  
335 the proposed MG; WECS, PV and BDG, is 3 MVA which provides a power supply for 5 MW load  
336 through the distribution network. Parameters of WECS and DE were derived from [29] and [19]  
337 respectively. The parameters of power electronic devices, low pass filter and line impedance are  
338 presented in Appendix.

339 This study focused on low-frequency critical modes, which significantly affect the MG stability.  
340 The low-frequency critical eigenvalues are mainly originated from the power-sharing controller in the  
341 frequency range of 2-10 Hz [8, 34]. According to participation factor analysis, active power, phase  
342 angle and reactive power state variables from PV and WECS contributed to modes of  $\lambda_{42,43}$  and  $\lambda_{45,46}$

343 respectively. It was also monitored that mode of  $\lambda_{42,43}$  has a damping ratio of 17.68% while  $\lambda_{45,46}$  is  
 344 characterized by 4.13% damping ratio. This indicated that the risk of instability from eigenvalues of  
 345  $\lambda_{45,46}$  is higher than that from  $\lambda_{42,43}$ . Moreover, since the investigated modes were situated closely,  
 346 similar state variables might participate in those neighbouring eigenvalues. It can be denoted that in this  
 347 situation, the eigenvectors of the corresponded modes might be similar [35]. As a consequence, the  
 348 interaction between those modes potentially occurred. The interaction event might lead to more  
 349 oscillatory conditions which result in deterioration of system damping or even unstable situations.

350 Trajectories of sensitive modes from RES based DG unit under variations of gain control  
 351 parameters are presented in this study. Small variation of droop gain, proportional and integral gain  
 352 control in a certain range are considered. Fig.6a shows root-locus of the investigated modes due to the  
 353 variation of active-power droop gain ( $n_p$ ) of PV and WECS. As  $n_p$  decreased, modes of  $\lambda_{42,43}$  moved to  
 354 the right, implies a deterioration of dynamic response. On the other hand, enhancement of oscillatory  
 355 condition was monitored indicated by the left movement of  $\lambda_{45,46}$ . Oscillatory frequency of  $\lambda_{45,46}$   
 356 drastically decreased from 7.408 rad/s or 1.17 Hz to 4.01 rad/s or 0.63 Hz at lower values of  $n_p$ . While  
 357 the frequency of mode  $\lambda_{42,43}$  did not change significantly around 10.682 rad/s or 1.701 Hz. Furthermore,  
 358 it was suggested that stability could be maintained if droop gains were set more than  $9.4 \times 10^{-6}$  rad/s/W.

359 Trajectories of sensitive modes due to the variation of reactive power droop gain ( $n_q$ ) s depicted  
 360 in Fig.6b. Enhancement of system dynamic response was monitored, designated by extensive left  
 361 movement of  $\lambda_{45,46}$  across the imaginary axis. Critical mode of  $\lambda_{42,43}$  was also influenced. The slight left  
 362 motion of the  $\lambda_{42,43}$  was observed during this variation. Moreover, system stability could be maintained  
 363 if the  $n_q$  was tuned less than  $2 \times 10^{-4}$  V/Var.

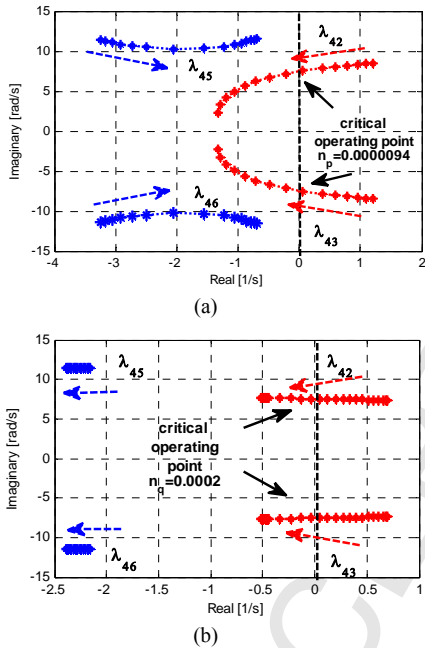


Fig. 6. Trajectories of sensitive modes when (a) active power droop gain ( $n_p$ ) varied from  $1.57 \times 10^{-5}$  rad/s/W to  $1.05 \times 10^{-6}$  rad/s/W and (b) reactive power droop gain ( $n_q$ ) varied from  $4.2 \times 10^{-4}$  V/Var to  $8.8 \times 10^{-5}$  V/Var.

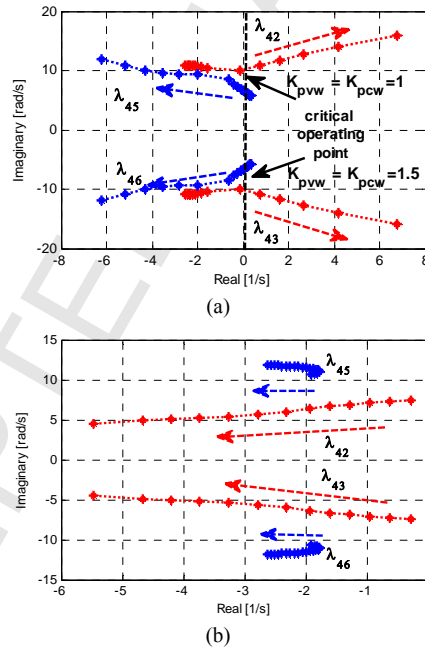


Fig. 7. Trajectories of sensitive modes when proportional ( $K_{pvw}, K_{pcw}$ ) (a) and integral ( $K_{ivpw}, K_{icw}$ ) (b) gains of WECS voltage and current controller were varied.

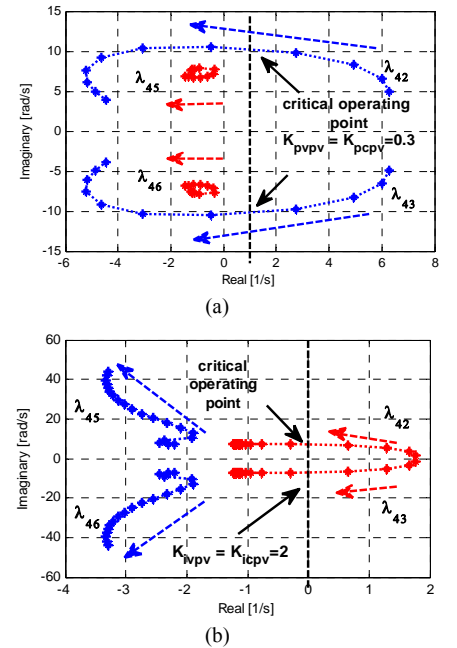


Fig. 8. Trajectories of modes when proportional ( $K_{pvv}, K_{pcv}$ ) (a) and integral ( $K_{ivv}, K_{icv}$ ) (b) gains of PV voltage and current controller were varied.

364 Investigation of low-frequency critical modes was then conducted by a varying gain of WECS  
 365 voltage ( $K_{pvw}$ ,  $K_{ivw}$ ) and current ( $K_{pcw}$ ,  $K_{icw}$ ) controller loops. As depicted in Fig. 7a, eigenvalues of  
 366  $\lambda_{42,43}$  departed toward left half plane due to  $K_{pvw}$  and  $K_{pcw}$  variations. Conversely, dynamic response of  
 367  $\lambda_{45,46}$  deteriorated significantly as  $K_{pvw}$  and  $K_{pcw}$  were varied. From this variation, system stability  
 368 boundary was determined. Stability could be maintained if  $K_{pvw}$  and  $K_{pcw}$  were tuned in the range of 1  
 369

370 to 1.5. Moreover, small-signal stability corresponded to DG units output power due to  $K_{ivw}$  and  $K_{icw}$   
 371 variations is shown in Fig.7b. As  $K_{ivw}$  and  $K_{icw}$  were varied the observed modes departed to the left.  
 372 This indicated damping enhancements of corresponded eigenvalues.

373 In Fig.8, different circumstances were observed as proportional ( $K_{pvpv}, K_{pcpv}$ ) and integral ( $K_{ivpv}, K_{icpv}$ )  
 374 gains of PV voltage and current control loops were varied. The trajectory of low-frequency critical  
 375 modes under  $K_{pvpv}$  and  $K_{pcpv}$  variations is shown in Fig.8a. Primarily, the eigenvalues of  $\lambda_{42,43}$  departed  
 376 to the left-hand side. However, as the gain controller was continuously increased, the investigated  
 377 modes of  $\lambda_{42,43}$ , start to move towards the imaginary axis, indicating deterioration of system dynamic  
 378 response. On the other hand, only small movement of modes of  $\lambda_{45,46}$  was monitored. Moreover, small-  
 379 signal stability corresponding to DG unit output power due to  $K_{ivpv}$  and  $K_{icpv}$  variations is shown in  
 380 Fig.8b. As  $K_{ivpv}$  and  $K_{icpv}$  were varied the observed modes departed to the left, indicating damping  
 381 enhancements of the system. To maintain a stable condition of PV output power,  $K_{pvpv}$  and  $K_{pcpv}$  should  
 382 be tuned more than 0.3 as depicted in Fig.8a. While, as shown in Fig.8b, the risk of instability  
 383 potentially occurred when  $K_{ivpv}$  and  $K_{icpv}$  were set less than 2.

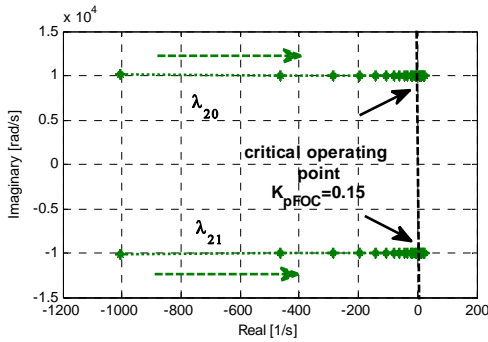


Fig 9. Trajectories of DC link voltage and current in WECS when the proportional gain of FOC ( $K_{pFOC}$ ) varied from 0.01 to 0.2.

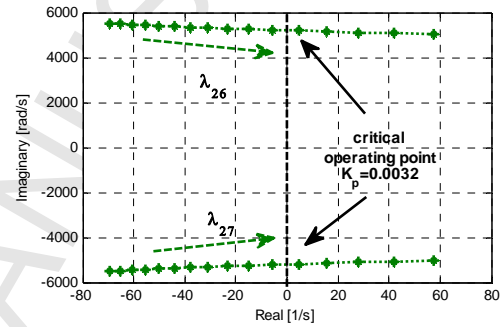


Fig 10. Trajectories of DC link voltage and current in PV system when DC link gain controller ( $K_{ppv}$ ) varied from 0.001 to 0.004.

384

385 Dynamic features of power electronic devices were characterized by higher frequency of  
 386 oscillation. The sensitive modes of these devices were represented by voltage and current of DC link  
 387 and inverter state variables. Fig. 9 represents root loci due to the variation of FOC gain. As the gain of  
 388 the controller varied, the modes corresponded to DC link voltage and current from WECS ( $\lambda_{20,21}$ ),  
 389 drastically moved toward imaginary axis, indicated deterioration of system stability. Moreover, it  
 390 was also observed that system be unstable if the proportional gain of FOC ( $K_{pFOC}$ ) was tuned above  
 391 0.15. Dynamic response of DC link voltage and current of PV ( $\lambda_{26,27}$ ) due to the variation of  
 392 proportional DC link control gain ( $K_{pDC}$ ) is shown in Fig. 10. It was clearly seen that as  $K_{pDC}$  increased,  
 393 system small-signal stability deteriorated severely. Instability possibly occurred when the  $K_{pDC}$  was  
 394 tuned beyond 0.0032.

### 395 B. Time-Domain Simulation

396 Time domain simulations in MATLAB Simulink environment were conducted to validate  
 397 previous eigenvalues analysis. Small perturbations of input variables associated with a voltage  
 398 reference of WECS ( $v_{ds}^*$ ) and PV ( $v_{dc}^*$ ) controller were applied to excite sensitive modes.

399 Fig.11 represents dynamic response of WECS and PV active power due to the variation of  $n_p$ .  
 400 According to the previous eigenvalues analysis, at  $n_p$  of  $7.32 \times 10^6$  rad/s/W, the output power of WECS  
 401 and PV had an oscillatory frequency of 7.408 rad/s or 1.17 Hz and 10.758 rad/s or 1.71 Hz, respectively  
 402 as shown in Fig.11a. Primarily, PV active power oscillated in the 0.58s time period or 1.72 Hz. While  
 403 WECS power output oscillated at 0.9s time period or 1.1 Hz. Since eigenvalues related to PV output  
 404 power has a higher damping ratio of 17.48%, the dynamic response subsided immediately. While lower  
 405 frequency around 1.1 Hz from WECS modes persisted until the stable operating point was achieved.

406 The critical operating point was experienced when  $n_p$  was tuned at  $9.35 \times 10^6$  rad/s/W as depicted  
 407 in Fig.11b. At this operating condition, WECS and PV active power oscillated continuously. Primarily,  
 408 PV output power oscillated at 0.6s time period or 1.67 Hz. According to root loci in Fig.6a, at the  
 409 critical points, positions of  $\lambda_{45,46}$  was closer to the imaginary axis than modes of  $\lambda_{42,43}$ , denote the less  
 410 damped condition of  $\lambda_{45,46}$  than  $\lambda_{42,43}$ . Hence, the oscillation associated to  $\lambda_{42,43}$  dissolved immediately  
 411 and then two modes started to oscillate together in the 0.9s time period or 1.1 Hz.

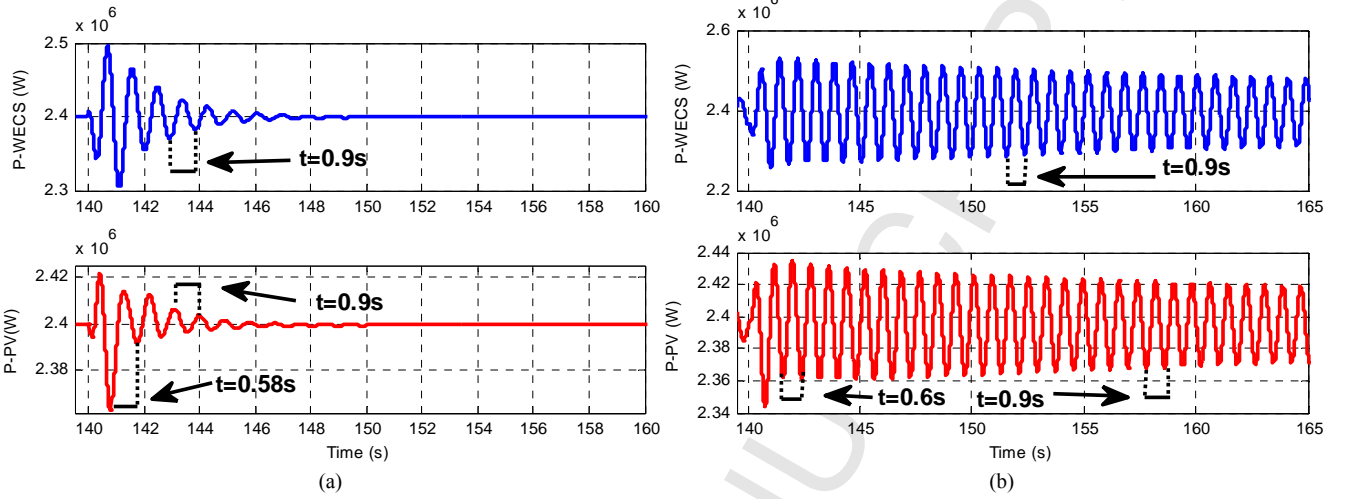


Fig. 11. WECS and PV active power at active droop gain ( $n_p$ ) of (a)  $7.32 \times 10^{-6}$  and (b)  $9.35 \times 10^{-6}$

### 412 C. Power Sharing and Small-signal Stability

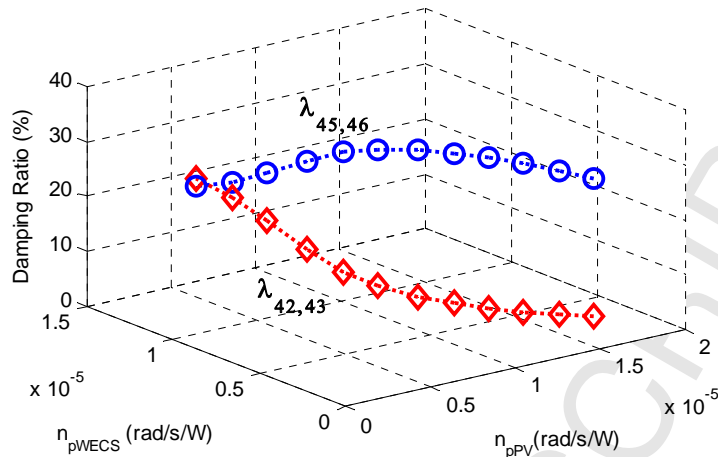
413 The dynamic behaviour of MG is not only influenced by the setting of gain parameters such as  
 414 droop, voltage and current controller gain but also influenced by parameters of the converter, line  
 415 impedances and load. Higher R/X ratio of line impedance result in more system damping hence it can  
 416 enhance the MG dynamic response. Conversely, increasing line resistance value affects the accuracy of  
 417 power-sharing and voltage profile within MG [8].

418 Converter parameters such as the inductance values and cut off frequency of low pass filter (LPF)  
 419 also influenced the dynamic responses of MG. A compromise between enhancing dynamic system  
 420 dynamic response and providing better harmonic rejection capability has to be considered in selecting  
 421 the LPF parameters [36]. Even though converter and line parameters influenced the MG stability  
 422 performance, those parameters can be considered constant according to their primary design. The  
 423 presented work is focused on the investigation of oscillatory conditions in a MG system under different  
 424 gain settings involving droop, voltage and current gain control settings. A detailed explanation of gain  
 425 control impact on MG stability is important since MG mostly powered by RES with fluctuating nature  
 426 characteristic. Therefore, proper gain control adjustments and settings should be better understood to  
 427 ensure accurate power-sharing and stable MG operation.

428 MG is demanded to deal with all possible power-sharing strategies. It was considered that  
 429 generated active power from WECS and PV were varied by gradually adjusting active power droop  
 430 gain in each DG unit. While lack of supplied power from those DG units is handled by BDG. In  
 431 practice, minimum allowable output from BDG is around 30% of its nominal rating (under-loading  
 432 operation of diesel engine less than 30 percent for extended periods can impact uptime and engine life).  
 433 Therefore, in this study it is considered that the diesel engine generator is operated around 30%-50% of  
 434 its nominal rating. Fig.12 shows damping ratio of sensitive modes in different power sharing schemes.  
 435 It was observed that at higher WECS and lower PV power-sharing, eigenvalues of  $\lambda_{42,43}$  and  $\lambda_{45,46}$  had  
 436 4.23% and 29.36% damping ratio respectively. MG dynamics response enhanced as power portion of



437 WECS and PV were decreased and increased respectively. The damping ratio of  $\lambda_{42,43}$  significantly  
 438 enhanced to 23.11%. While damping ratio of modes of  $\lambda_{45,46}$  decreased moderately to 21.86%.



439  
 440  
 441

Fig. 12. The damping ratio of the low-frequency critical modes in different power sharing schemes.

442 Fig.13 depicts MG dynamic responses associated with different power-sharing scheme among  
 443 DG units. The presented result confirmed the previous eigenvalues analysis in Fig.12. As shown in  
 444 Fig.13a, when MG was operated with dominant power from WECS and 40% nominal rating of BDG  
 445 (1.25 MW), less system damping was monitored. The less damping situation was reflected by more  
 446 oscillatory condition when the MG was subjected to small disturbance. Fig 13b presents equal  
 447 contribution from WECS and PV based DG units with BDG was operated at 45% of its nominal rating  
 448 (1.33 MW). From this figure, it can be observed that more damped situation than in Fig.13a was  
 449 monitored. Enhancement of system damping was further monitored when dominant power contribution  
 450 from PV and higher power injection from BDG (1.48 MW or 50% from its nominal rating) were  
 451 considered, as shown in Fig.13c.

452

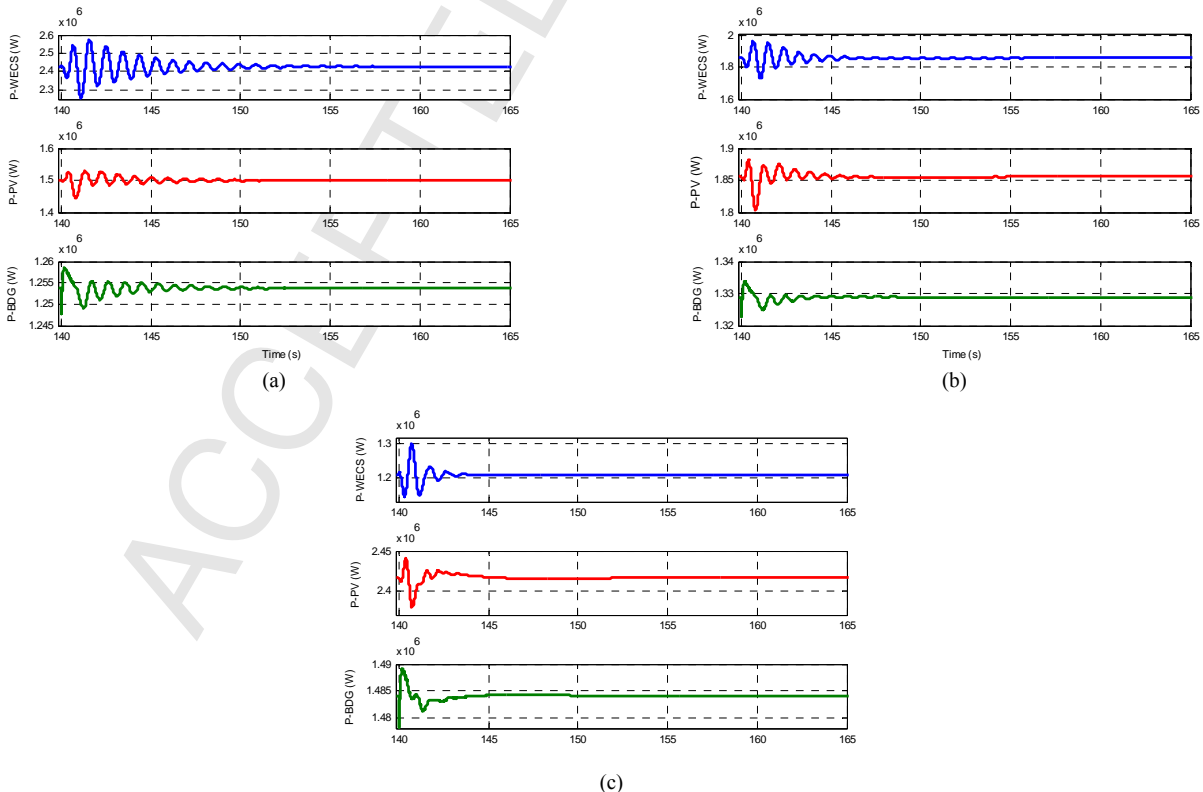


Fig. 13. Power sharing schemes in MG: (a) Dominant WECS, (b) Dominant PV and (c) Higher Contribution from BDG

#### D. Modal Interaction

The modal interaction could be a concern since it may cause a resonance phenomenon which deteriorated system stability. Interaction among neighbouring modes may emerge due to a variation of system parameter such as a gain controller, load changing and disturbance. Since modes of  $\lambda_{42,43}$  and  $\lambda_{45,46}$  situated closely, they could potentially interact. To investigate interaction scenarios, trajectories of the corresponded modes due to the variation of active power droop gain  $n_p$  in different WECS ( $K_{pvw}, K_{pcw}$ ) and PV ( $K_{pvpv}, K_{pcpv}$ ) voltage and current proportional gain tuning were investigated.

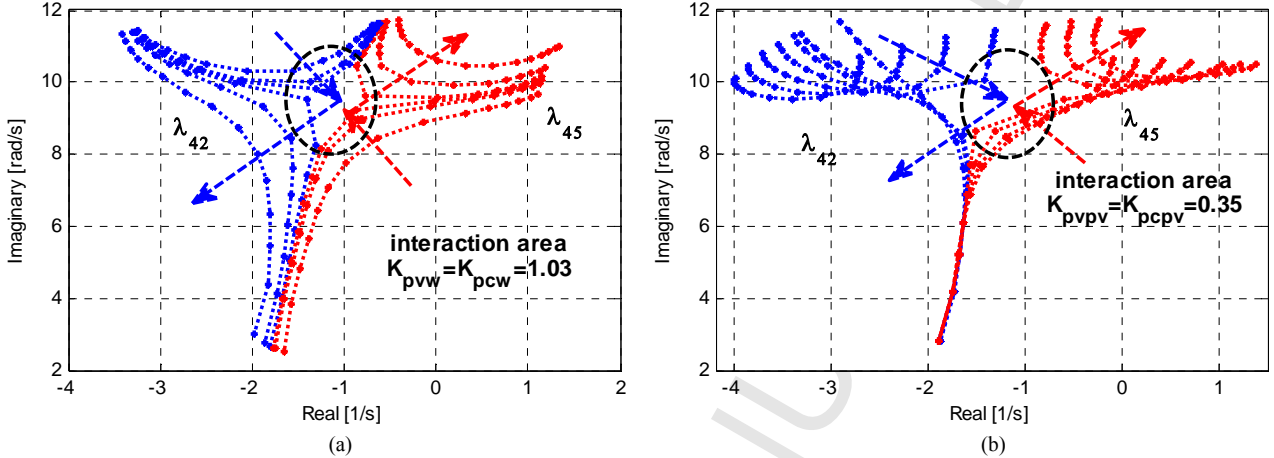


Fig. 14. Trajectories of modes due to the variation of active power droop gain in the various setting of (a) WECS and (b) PV control gains.

Fig.14 shows trajectories of investigated modes in different  $K_{pvw}, K_{pcw}$  and  $K_{pvpv}, K_{pcpv}$  setting during  $n_p$  variation. It was obviously shown that with similar  $n_p$  variation, different gain setting significantly influenced the eigenvalues movements. It was observed in Fig.14a, primarily, two eigenvalues came closer and interacted when  $K_{pvw}$  and  $K_{pcw}$  were tuned at 1.04. Around interaction point, as marked by a circle, those two modes moved oppositely. Modes of  $\lambda_{42}$  departed to the left while  $\lambda_{45}$  moved towards the right side of complex the plane, indicated enhancement and deterioration of system stability respectively. A similar trend was observed in Fig.14b. It was shown that after the interaction, PV modes moved to the right remarkably. Moreover, for lower  $n_p$ , the corresponded modes be unstable. The modal interaction emerged at  $K_{pvpv}$  and  $K_{pcpv}$  setting of 0.35.

The effect of modal interaction on the oscillatory condition in a MG system is visualised in time domain simulation as presented in Fig.15. The occurrence of modal interaction under variation of WECS gain control is depicted in Fig.15a. When proportional gains control of WECS ( $K_{pvw}, K_{pcw}$ ) were tuned at 1.01, the more damped situation was observed. In this gain control setting, the two investigated modes were far away from each other. Therefore, modal interaction did not take place. As the gains control of WECS and PV were tuned at 1.04, the more oscillatory condition was observed. At those particular gain setting, the two modes become closer and start to interact. Around an interaction point, as marked by a circle in Fig.14, the engaged modes were very sensitive to small parameter variations. When  $K_{pvw}$  and  $K_{pcw}$  were further increased to 1.06, a significant deviation of the root-loci was monitored. The two modes departed oppositely. One of the interacting modes departed to the left, yielded an enhancement of system oscillatory condition. While the other modes significantly moved toward the right-hand side of the complex plane. Those low-frequency modes which related to PV based DG unit dominantly affected the system stability. As a consequence, more damped condition subsided immediately and replaced by the less damped situation with similar oscillatory frequency as modes of PV.

485 A similar situation was monitored when PV gains control ( $K_{pvpv}, K_{pcpv}$ ) were varied. The  
 486 occurrence of modal interaction under variation of  $K_{pvpv}$  and  $K_{pcpv}$  is depicted in Fig.15b. Far from the  
 487 interaction point, when  $K_{pvpv}$  and  $K_{pcpv}$  were tuned at 0.31, the more damped situation was observed.  
 488 The modal interaction was identified at the setting of  $K_{pvpv}$  and  $K_{pcpv}$  of 0.35, indicated by the more  
 489 oscillatory condition. Around an interaction point, small perturbation or variation of system parameter  
 490 result in significant deviation of the engaged modes. One of the interacting modes departed remarkable  
 491 toward the right half-open plane, resulting in deterioration of the system stability. Severe deterioration  
 492 of the system dynamic response was identified. More oscillatory condition after interaction event due to  
 493 a significant decrease of damping ratio was reported.

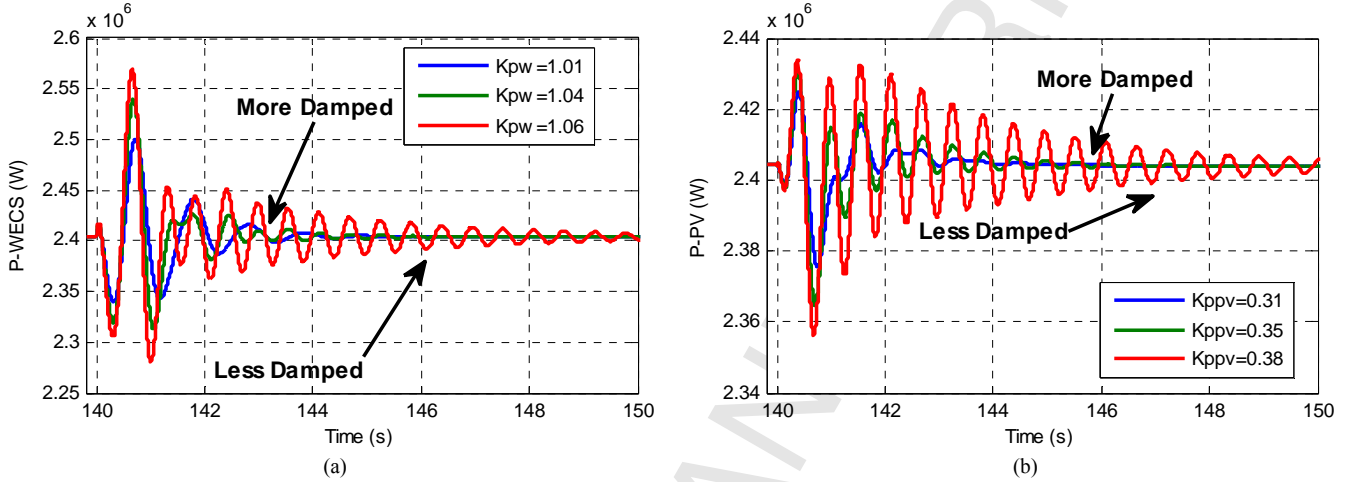


Fig. 15. (a) WECS and (b) PV active power influenced by modal interaction.

494

#### 495 4. Conclusions

496 A detailed small-signal model of a hybrid MG considering dynamics of power electronics devices  
 497 and its controllers was presented in this paper. Low and high-frequency critical modes corresponding to  
 498 DGs output power and converter state variables respectively, were significantly influenced by variation  
 499 of gain controllers. Since the different architecture of DG units provides distinct small-signal stability  
 500 features, evaluation of MG dynamic responses in many power-sharing strategies were investigated. The  
 501 eigenvalues analysis and time domain simulation suggested that at higher contribution of PV and BDG  
 502 based DG units, an enhanced system dynamic response was monitored. Moreover, the modal  
 503 interaction potentially happen due to the proximity of the low-frequency critical modes. It could be a  
 504 concern since it may cause resonance phenomenon which results in more oscillatory condition and lead  
 505 to system instability. Obtained result regarding the comprehensive analysis of small-signal stability in  
 506 autonomous operation of MG contributes to the design consideration and stability margin prediction of  
 507 hybrid MG system.

508 The modal analysis is sufficient to investigate the oscillatory stability in hybrid MG under small  
 509 variations of gain controllers. However, the presented method is not suitable for observing the dynamic  
 510 behaviour of the MG system when it was subjected to unbalanced situations. The time domain  
 511 simulation and Prony analysis methods are required for investigating the small signal stability  
 512 performance of MG under unbalance situations. Moreover, the uncertain condition of RES and load  
 513 have to be considered in investigating the MG stability. In future works, the effect of imbalance and  
 514 uncertainties circumstances will be investigated to provide more practical and realistic scenario of MG  
 515 operations.

516

517

518 **5. Appendix**

519

## System Parameters

520

Parameter	Symbol	Value
Rated Voltage	$V_{base}$	690 V
Parasitic resistance of DC/DC inductor	$R_b$	1m $\Omega$
DC/DC inductor	$L_b$	2mH
Parasitic resistance of DC/DC capacitor	$R_{cb}$	1m $\Omega$
DC/DC capacitor	$C_b$	1000 $\mu$ F
AC input side Inductance of AC/DC	$L_{sw}$	1mH
AC input side capacitor of AC/DC	$C_{inw}$	1000 $\mu$ F
AC Side Resistance of AC/DC converter	$R_{sdcw}$	10m $\Omega$
DC Side Capacitor of DC/AC converter	$C_{coutw}$	1000 $\mu$ F
DC Side Inductance of DC/AC inverter	$L_{sdcw}$	6.43mH
DC Link inductance	$L_{link}$	0.01mH
DC Link resistance	$R_{link}$	1m $\Omega$
DC Link Capacitance	$C_d$	6500 $\mu$ F
Low Pass Filter Inductance	$L_f$	1mH
Low Pass Filter Capacitance	$C_f$	100 $\mu$ F
Low Pass Filter Resistance	$R_f$	1m $\Omega$
Coupling Inductance	$L_c$	0.1mH
Coupling Resistance	$R_c$	1m $\Omega$
Load Resistance	$R_{lo}$	0.95 $\Omega$
Load Inductance	$L_{lo}$	10mH
Line Resistance (bus 1,2 and 3)	$R_{li}$	10m $\Omega$
Line Inductance (bus 1,2 and 3)	$L_{li}$	1mH

521 **6. References**

- 522 1. Gautam, D., V. Vittal, and T. harbour, *Impact of Increased Penetration of DFIG-Based Wind*  
523 *Turbine Generators on Transient and Small Signal Stability of Power Systems*. IEEE  
524 *Transactions on Power Systems*, 2009. **24**(3): p. 1426-1434.
- 525 2. Liu, H., et al., *Impact of High Penetration of Solar Photovoltaic Generation on Power System*  
526 *Small Signal Stability*, in *Power System Technology (POWERCON)*. 2010, IEEE: Hangzhou. p.  
527 1-7.
- 528 3. Zhou, W., et al., *Current status of research on optimum sizing of stand-alone hybrid solar-wind*  
529 *power generation systems*. *Applied Energy*, 2010. **87**: p. 380-389.
- 530 4. Shuai, Z., et al., *Microgrid stability: Classification and a review*. *Renewable and Sustainable*  
531 *Energy Reviews*, 2016. **58** p. 167-179.
- 532 5. Majumder, R., *Some Aspects of Stability in Microgrids*. *IEEE Transactions on Power Systems*,  
533 2013. **28**(3): p. 3243-3252.
- 534 6. Tang, X., W. Deng, and Z. Qi, *Investigation of the Dynamic Stability of Microgrid*. *IEEE*  
535 *transaction on Power System*, 2014. **29**(2): p. 698-706.
- 536 7. Control, I.-P.T.f.o.M., *Trends in Microgrid Control*. *IEEE Transaction on Smart Grid*, 2014.  
537 **5**(4): p. 1905-1919.
- 538 8. Hamzeh, M., et al., *Power Oscillations Damping in DC Microgrids*. *IEEE Transaction on*  
539 *Energy Conversion*, 2016. **31**(3): p. 970-980.
- 540 9. Rashidirad, N., et al., *A Simplified Equivalent Model for the Analysis of Low-Frequency*  
541 *Stability of Multi-Bus DC Microgrids*. *IEEE Transaction on Smart Grid*, 2017.
- 542 10. Bakic, V., et al., *Dynamical simulation of PV/Wind hybrid energy conversion system*. *Energy*,  
543 2012. **45**: p. 324-328.
- 544 11. Deng, W., X. Tang, and Z. Qi, *Research on Dynamic Stability of Hybrid Wind/PV System Based*  
545 *on Micro-Grid*, in *Electrical Machines and System ICEMS, International Conference on*. 2008,  
546 IEEE: Wuhan. p. 2627 - 2632

- 547 12. Nimpitiwan, N. and S. Kaitwanidvilai, *Static Output Feedback Robust Loop Shaping Control*  
548 *for Grid Connected Inverter using Genetic Algorithms*. International Journal of Innovative  
549 Computing, Information and Control, 2012. **8**: p. 6081-6093.
- 550 13. Kroutikova, N., C.A. Hernandez-Aramburo, and T.C. Green, *State-space model of grid-*  
551 *connected inverters under current control mode*. IET Electr. Power Appl., 2007. **1**(3): p. 329-  
552 338.
- 553 14. Katerei, F., M.R. Iravani, and P.W. Lehn, *Small-signal dynamic model of a micro-grid*  
554 *including conventional and electronically interfaced distributed resources*. IET Gen. Transm.  
555 Distrib., 2007. **1**(3): p. 369-378.
- 556 15. Krismanto, A., N. Mithulananthan, and K.Y. Lee, *Comprehensive Modelling and Small Signal*  
557 *Stability Analysis of RES-based Microgrid*, in *9th IFAC Symposium on Control of Power and*  
558 *Energy Systems CPES*. 2015, Elsevier: New Delhi, India. p. 282-287.
- 559 16. Pogaku, N., M. Prodanovic, and T.C. Green, *Modeling, analysis and testing of autonomous*  
560 *operation of an inverter-based microgrid*. IEEE Transactions on Power Electronics, 2007. **22**(2):  
561 p. 613-625.
- 562 17. Rocaber, J., et al., *Control of Power Converters in AC Microgrids*. IEEE Transaction on Power  
563 Electronics, 2012. **27**(11): p. 4734-4749.
- 564 18. Ugalde-Loo, C.E., J.B. Ekanayake, and N. Jenkins, *State-Space Modeling of Wind Turbine*  
565 *Generators for Power System Studies*. IEEE Transaction on Industry Application, 2013. **48**: p.  
566 223-232.
- 567 19. Krause, P.C., O. Wasynczuk, and S.D. Sudhoff, *Analysis of Electric Machinery and Drive*  
568 *System 2nd Edition*. 2002: Wiley-Interscience.
- 569 20. Middlebrook, R.D. and S. Cuk. *A General Unified Approach to Modelling Switching-Converter*  
570 *Power Stages*. in *Power Electronics Specialists Conference*. 1976. Cleveland.
- 571 21. Erickson, R.W. and D. Maksimovic, *Fundamental of Power Electronics Second Edition*. 2001,  
572 University of Colorado Boulder, Colorado: Kluwer Academic Publisher.
- 573 22. Wu, R., S.B. Dewan, and G.R. Slemon, *A Pwm Ac-to-Dc Converter with Fixed Switching*  
574 *Frequency*. Ieee Transactions on Industry Applications, 1990. **26**(5): p. 880-885.
- 575 23. Kahrobaeian, A. and Yasser Abdel-Rady I.Mohamed, *Analysis and Mitigation of Low-*  
576 *Frequency Instabilities in Autonomous Medium-Voltage Converter-Based Microgrids With*  
577 *Dynamic Loads*. IEEE Transaction on Industrial Electronics, 2014. **61**(4): p. 1643-1658.
- 578 24. ZHONG, Q.-C. and A.Y. ZENG, *Universal Droop Control of Inverters With Different Types of*  
579 *Output Impedance*. IEEE Access, 2016. **4**: p. 702-712.
- 580 25. Rahim, N.A. and J.E. Quaicoe. *Small Signal Model and Analysis of A Multiple Feedback*  
581 *Control Scheme for Three Phase Voltage Source UPS Inverter*. in *Proceedings of Power*  
582 *Electronics Specialist Conference*. 1996. Bovenno, Italy.
- 583 26. Munteanu, I., A.I. Bratcu, and N.-A.C.E. Ceang, *Optimal Control of Wind Energy System*. 2008,  
584 London: Springer-Verlag London Limited.
- 585 27. Wu, R., S.B. Dewan, and G.R. Slemon, *Analysis of an AC-to-DC Voltage Source Converter*  
586 *using PWM with Phase and Amplitude Control*. IEEE Transactions on Industry Application,  
587 1991. **27**(2): p. 12.
- 588 28. Anaya-Lara, O., et al., *Wind Generation: Modelling and Control*. 2009: John Wiley & Sons,  
589 Ltd.
- 590 29. BinWu, et al., *Power Conversion and Control of Wind Energy Systems*. 2011: Wiley.
- 591 30. Ugalde-Loo, C.E. and J.B. Ekanayake, *State-Space Modelling of Variable-Speed Wind Turbines:*  
592 *A Systematic Approach*, in *Sustainable Energy Technologies (ICSET)*. 2010, IEEE: Kandy, Sri  
593 Lanka. p. 1-6.
- 594 31. Kroutikova, N., C.A. Hernandez-Aramburo, and T.C. Green, *State-space model of grid-*  
595 *connected inverters under current control mode*. IET Electric Power Applications, 2007. **1**(3): p.  
596 329-338.
- 597 32. Barklund, E., et al., *Energy Management in Autonomous Microgrid Using Stability-Constrained*  
598 *Droop Control of Inverters*. IEEE Transaction on Power Electronics, 2008. **23**(5): p. 2346-2351.

- 599 33. Rese, L., A.S. Costa, and A.S.e. Silva. *Small-Signal Modeling and Analysis of Microgrids*  
600 *Including Network and VSI Dynamics*. in *Power Energy Society General Meeting*. 2012. San  
601 Diego: IEEE.
- 602 34. Vidyanandan, K.V. and N. Senroy, *Primary Frequency Regulation by Deloaded Wind Turbines*  
603 *Using Variable Droop*. IEEE Transaction on Power System, 2013. **28**(3): p. 837-846.
- 604 35. Padiyar, K.R., *Analysis of Subsynchronous Resonance in Power System*. 1999, New York:  
605 Springer Science.
- 606 36. Abusara, M.A., S.M. Sharkh, and J.M. Guerrero, *Improved droop control strategy for grid-*  
607 *connected inverters*. Sustainable Energy, Grid and Network, 2015. **1**: p. 10-19.

608

ACCEPTED MANUSCRIPT